Energy Storage Materials xxx (xxxx) xxx

Contents lists available at ScienceDirect

Energy Storage Materials

journal homepage: www.elsevier.com/locate/ensm

Hetero-layered MoS_2/C composites enabling ultrafast and durable Na storage

Zhenyou Li [a,b,*], Suya Liu [b,h], Bhaghavathi P. Vinayan [a], Zhirong Zhao-Karger [a,b], Thomas Diemant [c], Kai Wang [b,e], R. Jürgen Behm [a,c], Christian Kübel [a,b,d,e], Rüdiger Klingeler [f,g], Maximilian Fichtner [a,b]

[a] Helmholtz Institute Ulm (HIU) Electrochemical Energy Storage, Helmholtzstraße 11, D-89081, Ulm, Germany
[b] Institute of Nanotechnology (INT), Karlsruhe Institute of Technology (KIT), Hermann-von-Helmholtz-Platz 1, D-76344, Eggenstein-Leopoldshafen, Germany
[c] Institute of Surface Chemistry and Catalysis, Ulm University, Albert-Einstein-Allee 47, D-89081, Ulm, Germany
[d] Karlsruhe Nano Micro Facility (KNMF), Karlsruhe Institute of Technology (KIT), Hermann-von-Helmholtz-Platz 1, D-76344, Eggenstein-Leopoldshafen, Germany
[e] Department of Materials and Earth Sciences, Technical University Darmstadt, Alarich-Weiss-Straße 2, 64287, Darmstadt, Germany
[f] Kirchhoff Institute of Physics, Heidelberg University, INF 227, D-69120, Heidelberg, Germany
[g] Centre for Advanced Materials (CAM), Heidelberg University, INF 225, D-69120, Heidelberg, Germany
[h] International Center for New-Structured Materials (ICNSM), Laboratory of New-Structured Materials, State Key Laboratory of Silicon Materials, School of Materials Science and Engineering, Zhejiang University, Hangzhou, 310027, People's Republic of China

ARTICLE INFO

Keywords:
Interfacial engineering
Hetero-layered structure
SIBs
MoS_2/C composites
Heterointerfaces

ABSTRACT

Transition metal dichalcogenides have been considered as promising conversion-type electrode materials in sodium ion batteries, which allow multi-electron redox processes providing high capacities. However, the conversion reaction often leads to dramatic structural degradation of the electrodes during de-/sodiation, which strongly limits their cycle lifetime, achievable capacities and rate performances. To circumvent these obstacles, in this study, we applied an interfacial engineering strategy by constructing a MoS_2/C composite with an inter-overlapped hierarchical structure (MoS_2-C@C) through a bottom-up synthesis method. With the alternative stacking of MoS_2 and carbon layers, MoS_2-C@C provides an ideal environment to maintain the MoS_2 structure through the van de Waals interaction within the multilayers. At the same time, the heterointerfaces in MoS_2-C@C offer abundant electron transfer pathways. Consequently, the MoS_2-C@C electrode exhibits prominently improved electrochemical performance including a high reversible capacity of 590 mA h g^{-1}, a superior cycling stability up to 1000 cycles and an excellent rate capability (164 mA h g^{-1} at 20 A g^{-1} and 51 mA h g^{-1} at 50 A g^{-1}). The fast kinetics and high reversibility of the hetero-layered MoS_2/C composite for Na storage demonstrate the feasibility of this synthetic strategy to prevent the structural degradation of the conversion-type battery materials.

1. Introduction

Electrochemical energy storage (EES) system is an essential technology for effective utility of renewable sustainable energy sources. After decades of development, lithium ion batteries (LIBs) have become the most favourable EES devices for electric vehicles (EVs) and portable electronics [1,2]. However, the fast expansion of the market for EVs and grid-scale electricity storage raises the concern of the cost due to the limited cobalt and lithium reserves, which motivates to search for alternative and sustainable solutions [3–5]. Among various rechargeable batteries, sodium ion batteries (SIBs) have shown the most competitive electrochemical properties to LIBs. In addition, the sodium resource is earth abundant and evenly distributed all over the world, which renders SIBs promising as a post-lithium option [6]. Compared to Li^+, the size of Na^+ ion is ~35% larger (the radii for Li^+ and Na^+ are 76 and 102 p.m., respectively) [7], which may give rise to a higher diffusion energy barrier [8]. Furthermore, the sluggish ion diffusion could increase cell internal resistances, which possibly generate large amounts of heat inside the cell, causing not only large energy losses but also safety issues [9].

Conversion-type materials with multi-electron redox reaction could potentially deliver high capacity and high power density. Compared to intercalation chemistry, conversion-type reactions can circumvent the

* Corresponding author. Helmholtz Institute Ulm (HIU) Electrochemical Energy Storage, Helmholtzstraße 11, D-89081, Ulm, Germany.
E-mail address: zhenyou.li@kit.edu (Z. Li).

https://doi.org/10.1016/j.ensm.2019.05.042
Received 17 February 2019; Received in revised form 16 May 2019; Accepted 27 May 2019
Available online xxxx
2405-8297/

kinetic limitation induced by the large ionic size of Na^+ [10]. However, conversion reactions need to break the pristine chemical bonds and form entirely new products with completely different structures, which leads to huge volume changes during cycling, thus causing severe structural degradation [11]. More important, the desodiation process of conversion-based electrode is a series of solid state reactions between the multiple phase reduction products, usually with low reaction efficiency, thus restricting the reversibility of the electrochemical reactions. Besides, in case of metal sulfides, sodium polysulfides are presumably produced during the reactions, which could dissolve in the electrolyte and shuttle between the electrodes, causing further capacity fading [12]. In these regards, the development of appropriate conversion-type hosts with fast de-/sodiation kinetics and durable Na storage requires a special design of their structure, which could greatly alleviate the loss of the active materials as well as the segregation of the reduction products [13–15].

Interfacial engineering approaches are effective structural regulation methods, and have been proven to be especially suitable for two-dimensional structures such as MoS_2 [16]. As a typical conversion-type material, MoS_2 allows for electrochemical reaction with four-electron transfer per formula unit corresponding to a theoretical capacity of ~670 mA h g^{-1} for deep sodiation [17]. This makes it extraordinarily promising among the host candidates. Owing to the weak interlayer van der Waals interactions, the interfaces of MoS_2 can be designed even down to a single molecular layer level, either by modulating the interlayer distances or by introducing foreign species to build multilayer heterostructures [18–20]. By stacking the MoS_2 layers and the foreign 2D material layers in a defined sequence, a multilayer heterostructure may be more effective than pure interlayer expanded ones [21,22]. Taking a MoS_2:C heterostructure as an example, the inter-overlapped structure provides relatively stable expanded interlayer distances as well as individual MoS_2 layers [23]. As such, the elastic carbon layers sandwich each MoS_2 layer, serving as *in situ* protection layers for latter. Once the MoS_2 layer undergoes a destructive conversion reaction at low potential, the carbon layers can buffer the volume change and alleviate the dissolution of sodium polysulfides [16]. Moreover, the highly conductive carbon component could be homogeneously distributed in the composite structure, on a molecular layer level, which may compensate for the low conductivity of MoS_2 and the discharge product Na_2S, allowing for fast electrochemical reactions [24].

In this work, we report a facile interfacial engineering approach to construct a MoS_2:C inter-overlapped hierarchical structure (MoS_2-C@C) for ultrafast Na storage with long-term cycling stability. The superstructure was obtained by controlling a competing complexation and polymerization reaction between Mo precursor and dopamine. The strong protection effect of the inter-overlapped structure was highlighted by the superior battery performances of the MoS_2-C@C electrode to a simple carbon surface coated sample (carbon-coated composite, MoS_2@C) and an unprotected sample (multi-layered MoS_2, *m*-MoS_2). Further electrochemical measurements (CV and EIS), *in situ* Raman and the *ex situ* SEM characterization were applied to clarify structure-performance correlations. The results not only demonstrate the success of this route for this specific system, but, considering the easy complexation of dopamine with transition metal (TM) precursors, could also serve as a guideline for other layered TM-based superstructures.

2. Experimental methods

2.1. Materials synthesis

The MoS_2:C inter-overlapped hierarchical structure (MoS_2-C@C) was realized by an interfacial engineering approach [25]. Typically, α-MoO_3 nanorods were used as both Mo source and self-sacrificing template. The synthesis of the α-MoO_3 nanorods was adapted from the literature [26] with minor modifications: ammonium molybdate tetrahydrate ($(NH_4)_6Mo_7O_{24}{\cdot}4H_2O$, Sigma-Aldrich, 81%–83% MoO_3 basis) was treated in a 3 M nitric acid solution hydrothermally at 180 °C for 30 h. The resulting white powder was dispersed in a 2 mg mL^{-1} dopamine hydrochloride/tris-(hydroxymethyl)aminomethane buffer solution (10 mM, pH = 8.5) with an α-MoO_3/dopamine molar ratio of 1:3. The immediate colour change of the suspension from milky white to orange indicates the complexation of MoO_3 with dopamine. After ripening for at least 12 h, the solid was separated from the suspension and washed with H_2O and ethanol for 5 times. After that it was redispersed in an aqueous thiourea solution with a Mo/S molar ratio of 1:5. After stirring for 1 h, the solution was transferred into a 125 mL Teflon autoclave and reacted at 200 °C for 24 h. The final product was obtained by pyrolysis of the black powder obtained from the hydrothermal reaction in a stainless steel reactor under Ar atmosphere. A two-step sintering process was employed: first heating the sample to 350 °C for 1 h, then increasing the temperature to 800 °C and holding for 3 h.

The MoS_2@C nanorods (denoted as MoS_2@C) were synthesized by the same method as MoS_2-C@C but with a higher α-MoO_3/dopamine molar ratio of 2:1. For comparison, *m*-MoS_2 was also obtained by this approach, but without the addition of dopamine.

2.2. Characterization

The morphology and microstructure of the sample were characterized by scanning electron microscopy (SEM) and transmission electron microscopy (TEM). SEM secondary electron images were obtained using a ZEISS LEO 1530 at 15 kV. In order to increase the conductivity, the samples were prepared on a carbon tape followed by gold sputtering. For *ex situ* measurement, the samples were peeled off from the electrodes, which were washed thoroughly with ethanol and dried under vacuum overnight. In TEM studies, the imaging process was performed using an aberration (image) corrected FEI Titan 80–300 microscope operated at 300 kV, equipped with a Gatan UltraScan CCD camera. TEM samples were prepared by dispersing the powder in ethanol, placing a drop on copper grids (Quantifoil Inc.) and taking of the residual suspension after 30 min natural drying.

To obtain structural information, X-ray powder diffraction (XRD) was performed using a Bruker-AXS D8 diffractometer in a Bragg-Brentano geometry using Cu-Kα1 radiation ($\lambda = 1.541$ Å) with a step size of 0.02°. Thermal analysis of the samples was carried out with thermogravimetric analysis coupled with differential scanning calorimetry (TGA-DSC) in a Setaram SENSYS evo instrument. The measurement was conducted from room temperature to 700 °C under synthetic air flow with a heating rate of 5 °C min^{-1}. X-ray photoelectron spectroscopy (XPS) measurements were carried out in a PHI 5800 MultiTechnique ESCA system (Physical Electronic) using monochromatic Al K_α radiation (250 W, 13 kV), a detection angle of 45°, and pass energies of 93.9 and 29.35 eV for survey and detailed spectra, respectively. The C 1s line of the conductive carbon in the sample with a binding energy of 284.6 eV was used as internal reference.

Ex situ Raman spectra were collected in the spectral range of 100–3000 cm^{-1} by using an inVia™ confocal Raman microscope (RENISHAW) with a 532 nm excitation laser. In the confocal system, a grating was used as dispersion element with a groove density of 2400 mm^{-1}, while a slit of 65 μm was applied to focus the laser in one dimension, centering at 1859 μm. *In situ* Raman measurements were conducted using an ECC-Opto-Std (EL-CELL® GmbH) electrochemical cell connected with Raman microscope. The cathode side of the cell was sealed with a thin optical glass window (0.15 mm) and made air-tight with a rubber seal. The battery tester was an Interface 1000TM Potentiostat/Galvanostat/ZRA (Gamry Instruments, Inc.) electrochemical workstation with "Gamry Echem Analyst" software. The cell was galvanostatic cycled at 0.1 A g^{-1}. The laser power was kept below 5 mW to avoid the decomposition of the sample. With an autofocus function, the probed sample spot was continuously focused during the experiment. Every spectrum was recorded as average of 3 scans of 10 s each.

2.3. Electrochemical measurements

All electrochemical studies except for electrochemical impedance spectroscopy (EIS) were carried out using a two-electrode Swagelok cell configuration. The cathode was made by coating a copper foil with a slurry containing 70% active material, 20% Super P (Timcal) and 10% carboxymethyl cellulose (CMC) in *N*-methyl-2-pyrrolidone (NMP), followed by vacuum drying at 80 °C for 15 h. A typical mass loading of the active material was 1.0–1.5 mg cm^{-2}. The cells were assembled in an Ar-filled glovebox (both H_2O and $O_2 < 0.5$ ppm) using 1 M $NaClO_4$ in propylene carbonate (PC) with 5 wt% fluoroethylene carbonate (FEC) as electrolyte, Na foil as counter electrode and glass fibre as separator. For the EIS measurements, a three-electrode Swagelok cell configuration was used with the same working electrode and counter electrode mentioned above and Na wire as reference electrode. Cyclic voltammetry (CV) and EIS measurements were performed using a VMP3 multichannel potentiostat (Bio-Logic SAS), while for galvanostatic cycling we used an Arbin battery cycling unit. EIS data were analysed with the help of the Z Fit function of the EC-Lab software. All cells were running in a voltage range of 0.01–3.0 V vs. Na/Na^+.

3. Results and discussion

3.1. Synthesis strategy & characterization of MoS_2/C composites

As a member of the catecholamine and phenethylamine families, dopamine not only exhibits a robust adhesion to many surfaces, but also offers strong ionic coordination bonds to various transition metal ions [27]. The adhesion is based on the abundant functional groups and the reductive nature of dopamine, which induces easy self-polymerization in aqueous solution. The complexation, however, is triggered by the catechol groups with affinity to the metal ions [28]. Inspired by the properties of dopamine, we design the MoS_2-C@C superstructure in this work by controlling the competing self-polymerization and the complexation with Mo(VI) precursors as illustrated schematically in Fig. 1. A previous report showed that the formation of catecholato-iron complexes and the degree of complexation strongly depend on the metal/catechol group ratio in solution [29]. We believe that this should also apply to the dopamine-molybdenum system. At low MoO_3/dopamine molar ratio (1:3), each Mo atom tends to coordinate with more than one dopamine molecule due to the excess of dopamine. The dopamine ligands are likely to donate their electrons to the Mo atoms, inducing self-polymerization of dopamine [30]. The multi-complex (preferably six coordination of Mo, corresponding to tri-complex) [29] helps to break down the nanorods of MoO_3, thus enabling coordination of the inner Mo atoms, resulting in a polydopamine (PDA)-MoO_3 complex [30]. According to XRD patterns in Fig. S1a, the long-range ordering of the MoO_3 has been broken with the addition of excess amount of dopamine, resulting in an almost amorphous structure of the MoO_3/dopamine tri-complex. Meanwhile, tremendous morphology change from rod-like to plate-like shape has been observed in the corresponding SEM images in Fig. S1. During hydrothermal treatment, the tri-complex reacts with H_2S, which is generated from thiourea, to form MoS_2 nuclei in between the PDA layers followed by the growth of layered MoS_2 nanosheets. After annealing the PDA layers, the designed inter-overlapped structure is obtained. According to Ref. [29], at a high MoO_3/dopamine molar ratio of 2:1, each Mo atom prefers to coordinate with only one dopamine molecule. This mono-complex promotes dopamine adhesion on the MoO_3 surface leading to the formation of PDA coated MoO_3 nanorods. With the PDA coating, the rod morphology could be kept even after hydrothermal treatment, i.e., the MoS_2@C nanorods were obtained after the same sintering process. For comparison, the pure MoS_2 sample (*m*-MoS_2) was also produced with the same procedure without addition of dopamine.

The morphology of the MoS_2/C composites was characterized by SEM and TEM. The representative SEM image of the MoS_2-C@C (Fig. 2a) shows some nanosheet assemblies with several hundred nm in size. The high resolution TEM (HR-TEM) image (Fig. 2d) reveals the MoS_2 nanosheets consisting of a few layers with a spacing of ~1.00 nm, significantly expanded compared to the (002) plane spacing of 0.62 nm in bulk MoS_2. The nanosheets are coated by a ~2 nm-thick amorphous layer, which presumably originates from carbonization of the PDA coating. The MoS_2@C sample exhibits a porous rod morphology with ~600 nm in diameter as seen from the SEM image in Fig. 2b. The porous structure consists of nanosheets with around 3–6 layers thick (Fig. 2e). The interlayer distance of MoS_2@C was determined to be ~0.68 nm, which is slightly larger than the bulk MoS_2 (002) lattice distance and fits to the

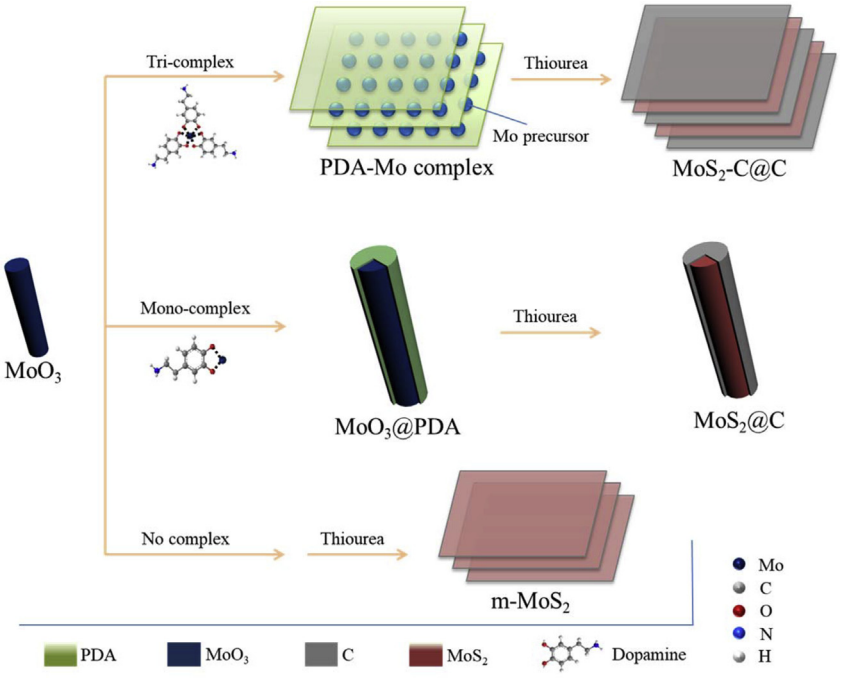

Fig. 1. Schematic illustration of the synthesis strategies for the MoS_2/C composites.

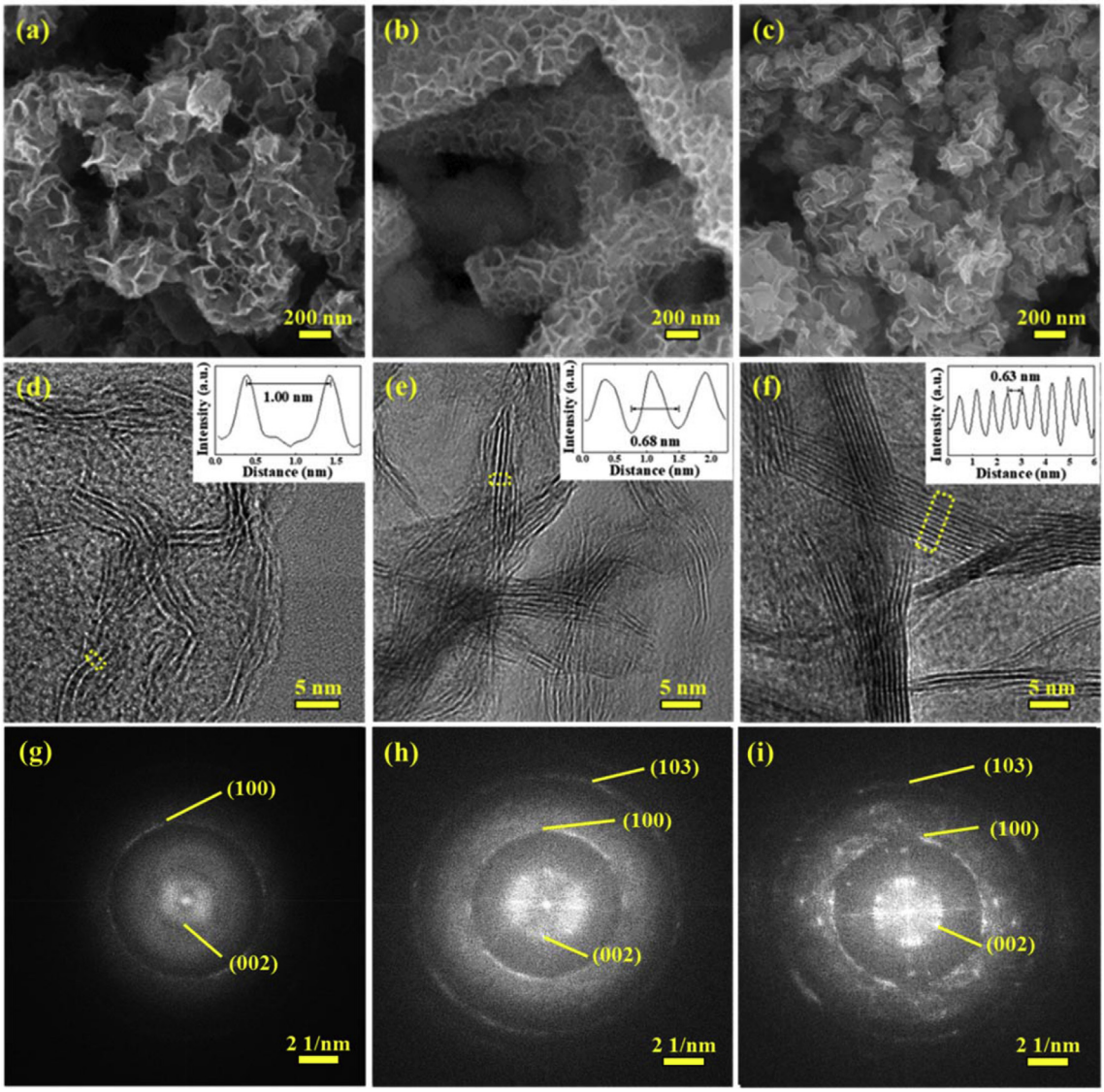

Fig. 2. Morphology of the MoS_2/C composites: SEM and HR-TEM images of MoS_2-C@C (a) and (d), MoS_2@C (b) and (e), and *m*-MoS_2 (c) and (f). The line profile within the boxes in (d)–(f) marked by the dotted yellow lines are shown as inset of each image, illustrating the interlayer distances of each sample. (g)–(i) present the FFT images of Fig. S2 (MoS_2-C@C), (e) and (f), respectively. (For interpretation of the references to colour in this figure legend, the reader is referred to the Web version of this article.)

slightly wrinkled appearance of the MoS_2 sheets, indicating a high local defect density. The Fast Fourier Transform (FFT) image of the surface zone (Fig. S3b) exhibits a typical hexagonal pattern of carbon, suggesting the surface carbon coating of the MoS_2@C sample. In case of *m*-MoS_2, the sample also shows a layered structure (Fig. 2c), but with relative loose interaction between each nanosheet. The corresponding HR-TEM image (Fig. 2f) demonstrates that the nanosheet consists of a well-defined stack of multiple MoS_2 molecular layers with interlayer distances of ~0.63 nm, close to the bulk value. Fig. 2g–i presents FFT patterns extracted from Fig. S2 (MoS_2-C@C), Fig. 2e (MoS_2@C) and Fig. 2f (*m*-MoS_2), respectively. In the FFT pattern of the MoS_2-C@C sample, the smaller (00*l*) rings relate to the interlayer expansion while the absence of the (103) ring indicates the distortion of the MoS_2 layers [31,32]. With small particle size and low crystallinity, the MoS_2-C@C structure yields a much higher surface area of 220 $m^2 g^{-1}$ compared to MoS_2@C (88 $m^2 g^{-1}$) and *m*-MoS_2 (44 $m^2 g^{-1}$) samples (see Fig. S4). Furthermore, there are plenty of micro- and mesopores in the inter-overlapped structure while less pore volume and larger pore size in the other two samples. The high surface area and abundant pores are believed to be beneficial for fast and durable electrochemical reactions, which will be discussed in the following section.

The structure and chemical state of the three MoS_2/C composites was further examined in more detail by XRD, Raman spectroscopy and XPS. In Fig. 3a, all diffraction peaks of the *m*-MoS_2 and the MoS_2@C samples could be indexed by the standard pattern of 2H-MoS_2, indicating the successful synthesis of the MoS_2 species. Compared to the *m*-MoS_2, the diffraction peaks of the MoS_2@C sample are broader with lower intensity, which may suggest the existence of a carbon coating. Particularly, the (002) peak at ~13.2° is shifted to lower angle, in agreement with the slightly expanded few layer feature resolved by TEM imaging (Fig. 2e). The XRD pattern of the MoS_2-C@C sample generally agrees well with those of the other two samples. Only for the (002) peak, two broad halos are observed at 8.7° and 16.4° in the XRD pattern of the MoS_2-C@C sample, which is different from the other two samples. The first halo corresponds to an interlayer distance of 1.01 nm, which is identical to the value determined from the crystal lattice of the TEM image. The largely expanded interlayer distance cannot be attributed to a simple interlayer expansion or intercalation of small molecules (e.g. NH_3) because it is thermally stable at 800 °C under argon atmosphere [33]. Instead, it relates more likely to a carbon layer in between the MoS_2 layers.

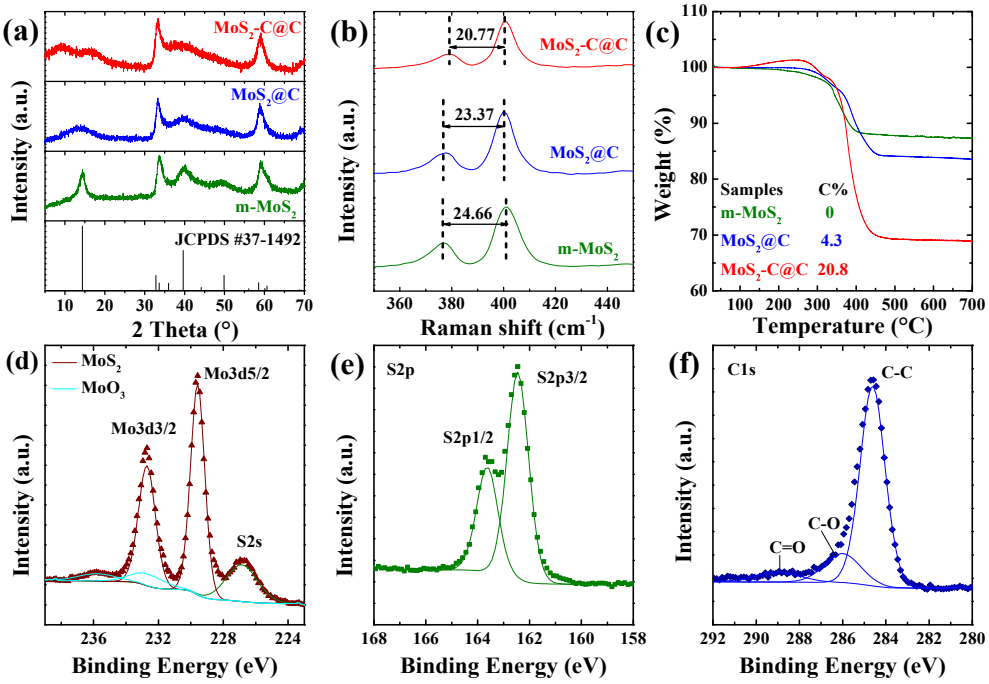

Fig. 3. Structural and chemical characterization of the MoS_2-based nanostructures: XRD (a), Raman spectra (b), and TGA (c) of MoS_2-C@C, MoS_2@C and *m*-MoS_2; XPS detail spectra of MoS_2-C@C in the Mo3d (d), S2p (e), and C1s (f) regions.

Considering the alternative stacking of a carbon monolayer (d = 0.34 nm) and a MoS_2 (d = 0.62 nm) monolayer, the distance between neighboring MoS_2 layers would be expected to be 0.96 nm, which is close to our diffraction data [19]. Supporting this hypothesis, the second halo (16.6°) could be explained by a higher order reflection of (00*l*) planes. This assumption was checked by Raman spectroscopy because the intralayer bonding and lattice dynamics are affected even by weak interlayer interactions. In case of MoS_2, the difference between the E^1_{2g} mode (~380 cm^{-1}) and the A_{1g} mode (~400 cm^{-1}) is an indicator for the number of stacked layers. In Fig. 3b, the value for the MoS_2-C@C sample is 20.8 cm^{-1} corresponding to 1–2 layers of MoS_2 according to literature [34]. This value is much smaller than that of the MoS_2@C sample (23.4 cm^{-1}, 3–4 layers) and the *m*-MoS_2 sample (24.7 cm^{-1}, >6 layers). The quasi monolayer feature of the MoS_2-C@C sample is in line with our assumption that there are carbon layers in between. The carbon layer shields the strong van der Waals interaction between the MoS_2 sheets. Hence, the MoS_2-C@C sample shows a monolayer-like behavior in Raman spectra due to the unique inter-overlapped structure [35].

In the high wave number region of the Raman spectra (see Fig. S5), the characteristic peaks of the D and G bands of carbon are detected for both the MoS_2-C@C and the MoS_2@C samples, but not for *m*-MoS_2. This indicates the presence of carbon species in the MoS_2/C composites. The carbon content of the MoS_2/C composites was further analysed by TGA-DSC using air as carrier gas. From the TGA curves in Fig. 3c, there is 20.8% carbon in the MoS_2-C@C while it is only 4.3% carbon in the MoS_2@C. In the DSC curves (Fig. S6), the first peaks for all samples are related to the oxidation of MoS_2 to MoO_3 while the second peaks for MoS_2-C@C and MoS_2@C correspond to carbon oxidation. It should be noted that both onsets as well as exothermic peak positions occur at lower temperature in MoS_2-C@C than in MoS_2@C. This suggests a higher reactivity of both the MoS_2 and the carbon component in the former sample, which might result from the low crystallinity of the sample due to the inter-overlapped structure.

From the XPS spectra in Fig. 3d–e and Fig. S7, the Mo3d and S2p signals show typical MoS_2 features with trace amount of MoO_3 signals in all samples, indicating a similar chemical state of MoS_2 in all three samples. In addition, carbon signals are also observed in the XPS spectrum of MoS_2-C@C (Fig. 3f) with peaks at 284.6, 286.1 and 288.8 eV, which are assigned to C-C, C-O and C═O groups, respectively. A similar C1s spectrum was obtained for the MoS_2@C sample (Fig. S7c). The carbon signals can be related to the carbon component in MoS_2@C and MoS_2-C@C. However, carbon signals are also detected in the *m*-MoS_2

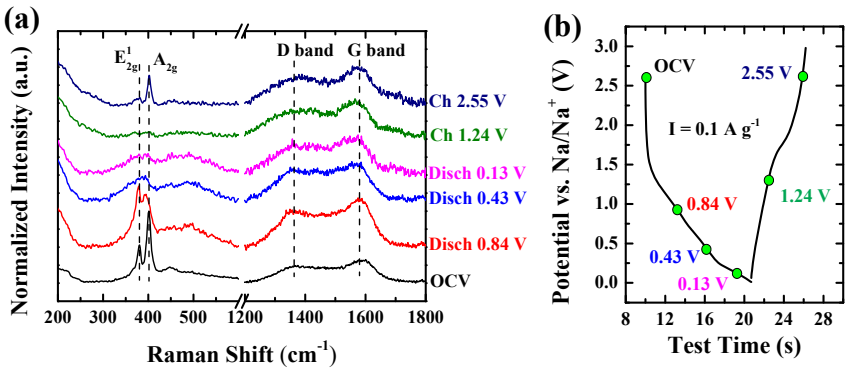

Fig. 4. *In situ* Raman measurement of MoS_2-C@C electrode at 1st cycle: (a) Raman spectra; (b) corresponding charge-discharge curve.

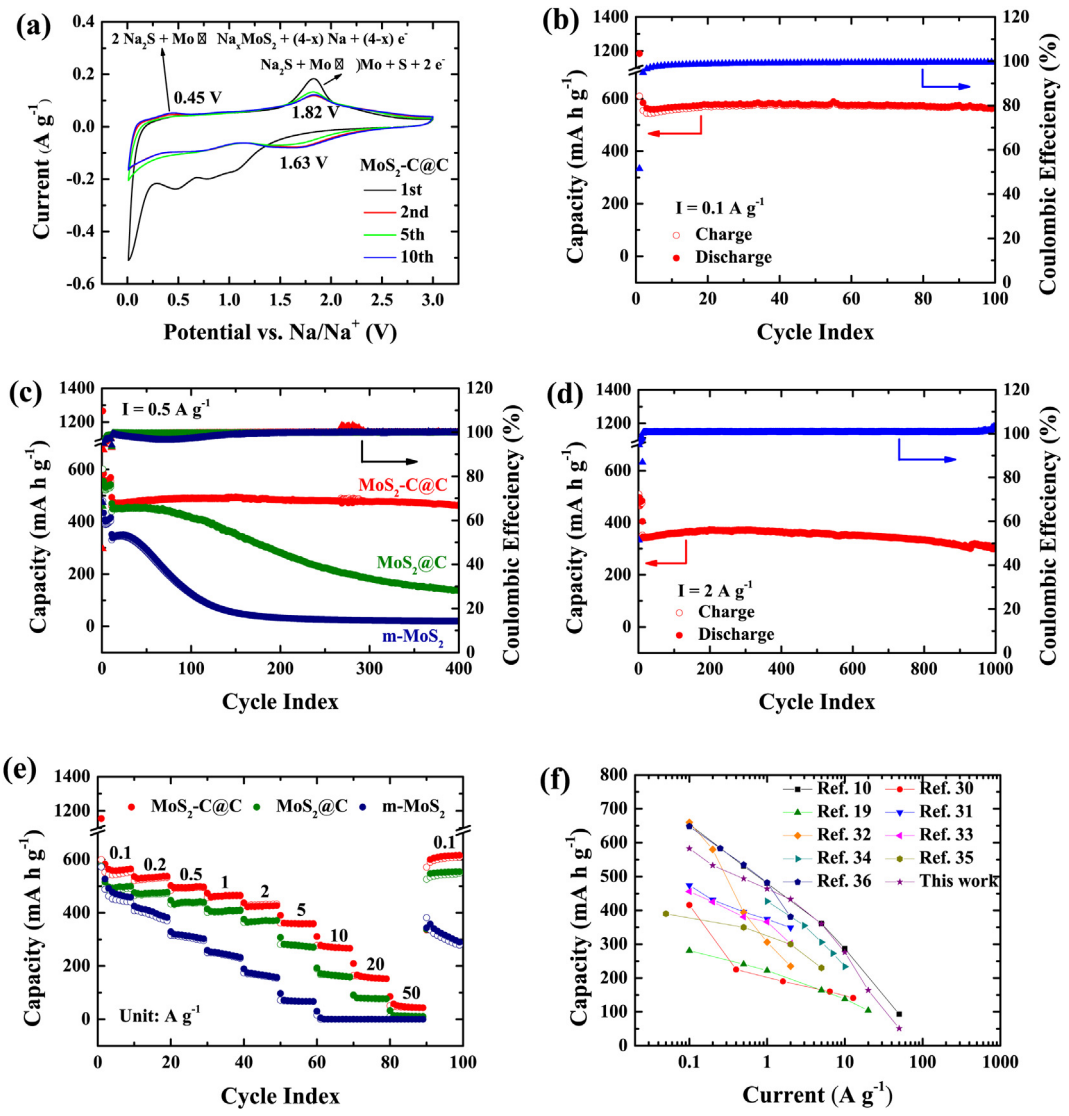

Fig. 5. Electrochemical performance of the MoS_2-C@C: (a) CV curves at 0.1 mV s^{-1}; (b) galvanostatic cycling at 0.1 A g^{-1} (corresponding charge-discharge profiles are shown in Fig. S8); (c) galvanostatic cycling at 0.5 A g^{-1} and comparison with MoS_2@C and *m*-MoS_2 (corresponding charge-discharge profiles are shown in Fig. S9); (d) long-term cycling stability at 2 A g^{-1} (corresponding charge-discharge profiles are shown in Fig. S10); (e) rate capability at 0.1–50 A g^{-1} and comparison with MoS_2@C and *m*-MoS_2 (corresponding charge-discharge profiles are shown in Fig. S11); (f) comparison of the rate capability between the MoS_2-C@C and recently reported, state-of-the-art MoS_2-based electrodes [9,20,40,41,43–47]. All cells in (c) and (d) were running at 0.1 A g^{-1} for 10 cycles before applying a higher current.

sample (Fig. S7f), which are attributed to the C-containing adsorbed species on the surface of the sample.

Overall, the characterization data confirms the assumption of a MoS_2-C@C inter-overlapped structure, where a layer of MoS_2 alternates with a layer of carbon, thus forming a sandwich structure with alternating chemical, electrochemical, and electric properties.

3.2. *Electrochemical performances & fast Na storage*

The electrochemical Na storage mechanism in MoS_2-C@C was firstly investigated using *in situ* Raman spectroscopy within a potential range of 0.01–3.0 V, which is beyond the pure intercalation range [36]. Fig. 4a shows the Raman spectra collected at various states of charge in the first galvanostatic cycle, while Fig. 4b presents the corresponding charge-discharge curve. Therein, the Raman spectrum of the MoS_2-C@C electrode at open circuit voltage (OCV) displays identical fingerprint features of 2H-MoS_2 (the E^1_{2g} and A_{1g} modes) and the typical peaks of carbon species (D/G bands) as that of the as-prepared powder sample (cf. Fig. 3b). When discharging the cell to 0.84 V, the E^1_{2g} peak becomes more prominent than the A_{1g} peak. The peak evolution could be attributed to the electron doping to 2H-MoS_2 during Na^+ ions intercalation, leading to a significant change of the out-of-plane (A_{1g}) mode but a weak influence on the in-plane (E^1_{2g}) mode [37]. Deep discharging to 0.43 V and 0.13 V results in the disappearance of the characteristic peaks of 2H-MoS_2, corresponding to its structural change, which might indicate the 2H to 1T phase transition and the transformation of MoS_2 to metallic Mo and Na_2S [38]. In the reverse charge process, the E^1_{2g} and A_{1g} peaks reappear at 2.55 V but with lower intensity, which implies the partial reformation of 2H-MoS_2.

The whole redox process is also evident in the CVs in Fig. 5a. In the first reduction scan of the CV, the double peak at 1.05 and 0.85 V corresponds to the intercalation of Na^+ [39], while the sharp peak at ~0.1 V is probably related to the transformation of MoS_2 to metallic Mo and Na_2S nanoparticles [40]. Additionally, another peak at 0.5 V might suggest the formation of a solid electrolyte interphase (SEI) [41]. In the following cycles, almost all the features of the first reduction scan disappear, indicating a strongly irreversible transformation process. Instead, a new pair of peaks appears at 1.63/1.82 V, which is assigned to

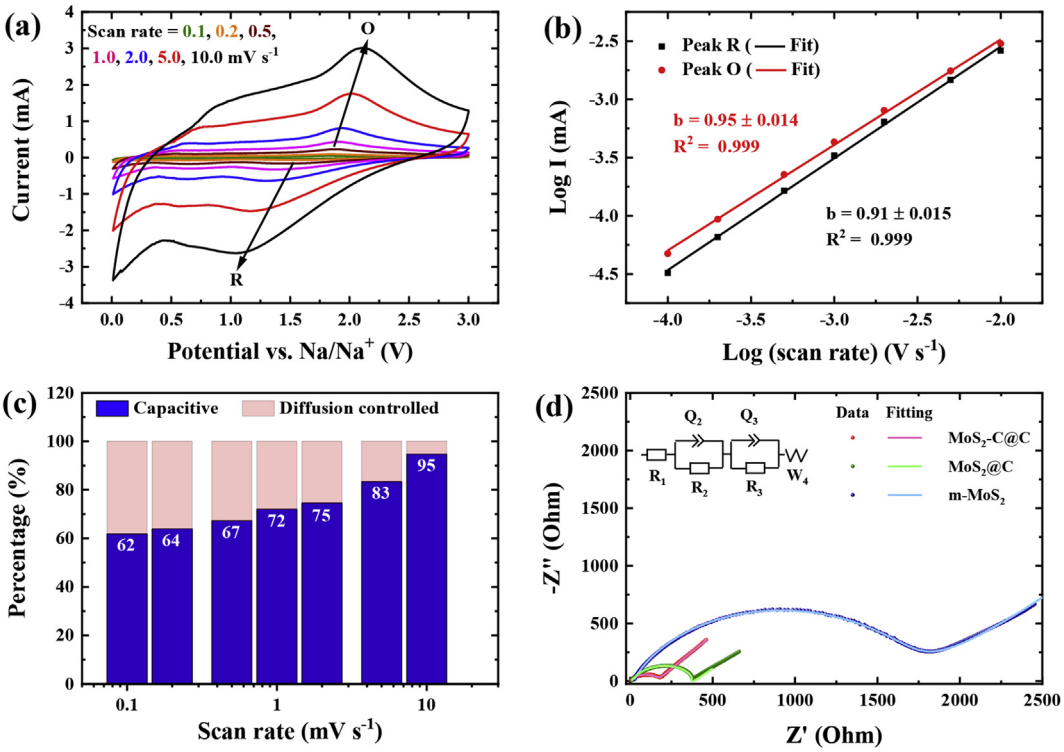

Fig. 6. (a) CV curves of MoS_2-C@C at different scan rate; (b) current response versus scan rate (log I vs. log(scan rate)) plots of the redox peaks; (c) capacitive and diffusion controlled contributions to the electrochemical processes at varying scan rates; (d) Nyquist plots of MoS_2-C@C, MoS_2@C and *m*-MoS_2 at OCV. The inset shows the equivalent circuit used for fitting.

the redox reaction between NaS_2 and S [36,42]. Although the conversion reaction seems to be irreversible to a large extent, there is still a tiny oxidation peak at 0.45 V, which relates to the reformation of a small amount of Na_xMoS_2. In this case, the formation of S and Na_xMoS_2 are competing reactions during charging process. Due to the low reaction efficiency between two solid phases (i.e., Mo and Na_2S), the latter is usually hindered. Therefore, the appearance of the reformation peak is an indicator for good dynamic properties (particle size and electric conductivity etc.) of the MoS_2-C@C electrode. Nevertheless, both the dis-/charge curves and the CVs are quite identical from the second cycle on, demonstrating a reversible and durable Na storage.

Fig. 5b shows the galvanostatic cycling stability of the MoS_2-C@C electrode at a low current rate of 0.1 A g^{-1}. It delivers a high initial discharge capacity of ~1200 mA h g^{-1}. In the following first charging process, the capacity drops to ~600 mA h g^{-1}, resulting in a coulombic efficiency of 52%. Nevertheless, the capacity keeps stable after the initial drop, with a high coulombic efficiency (>99%) for up to 100 cycles. The irreversible capacity loss in the first cycle is mainly attributed to the partially irreversible conversion reaction and the formation of a solid electrolyte interphase (SEI) [38], which is consistent with the CV data. The superior electrochemical performance of MoS_2-C@C is illustrated by comparing with the results of the MoS_2@C and *m*-MoS_2 electrodes. In Fig. 5c, the electrode with inter-overlapped structure exhibits a stable capacity of 463 mA h g^{-1} after 400 cycles, corresponding to a capacity fading rate of 0.016% per cycle. In contrast, for the MoS_2@C electrode, the capacity remains stable at ~450 mA h g^{-1} only for less than 100 cycles and decreases after that to 138 mA h g^{-1} in the 400th cycle (0.18% decay per cycle). The *m*-MoS_2 electrode shows even worse results. Here, a stable capacity of ~351 mA h g^{-1} is maintained for only 20 cycles. Afterwards, it quickly drops to around 20 mA h g^{-1}, which is mainly attributed to the contribution of the carbon black additive. The capacity fading possibly correlates to the reaction kinetics from Na_2S to S or MoS_2, which is also a general issue in Na-S battery systems [48]. Fig. S9d shows the comparison of overpotentials of the three MoS_2-based samples, determined by the difference of average charge and discharge potentials. The polarization of *m*-MoS_2 is increasing from ~0.7 V to more than 1.5 V with respect to cycle, while the value of MoS_2-C@C keeping almost unchanged at ~0.7 V. A detailed discussion of the structure-performance correlation will be given later in this paper. Moreover, the long-term cycling stability of MoS_2-C@C was tested at 2 A g^{-1} (see Fig. 5d). After first few cycles, the capacity stays almost unchanged for up to 1000 cycles (312 mA h g^{-1} at 1000th cycle), demonstrating the excellent cycling stability. Importantly, the MoS_2-C@C electrode shows not only an excellent cycling stability but also a superior rate capability. As shown in Fig. 5e, the MoS_2-C@C electrode gives high capacities of 583, 533, 494, 464, 433, 360 mA h g^{-1} at current rates of 0.1, 0.2, 0.5, 1, 2, 5 A g^{-1}, while the capacities of the other two samples quickly drop with increasing current. The inter-overlapped structure is even capable to accept ultra-high current rates of 10, 20, 50 A g^{-1}, offering capacities of 276, 164 and 51 mA h g^{-1}. In contrast, the MoS_2@C electrode only provides half or even less of the capacity at corresponding currents while the *m*-MoS_2 electrode shows almost no capacity at all. The long-term cycling stability and excellent rate capability of the MoS_2-C@C electrode are further highlighted by comparing with the results of other studies on state-of-the-art MoS_2-based SIBs anodes. As shown in Fig. 5f and Table S1, the battery performance of the MoS_2-C@C superstructure is superior to most of the MoS_2-based SIBs anodes, making it a promising candidate for potential application in high-performance SIBs.

In order to get more insight into the correlations between structure and battery performance, we performed further electrochemical measurements. Fig. 6a shows the CVs of a MoS_2-C@C electrode at different scan rates, which result in curves with similar shape and increasing current response with increasing scan rate. The main reduction peaks at 1.0–1.5 V and oxidation peaks at 1.7–2.2 V, which correspond to the transformation between the Na_2S/S redox pair, are fully preserved even at high scan rates. The other oxidation peaks at 0.45–0.88 V, which relate to the reformation of Na_xMoS_2, also retain at 10 mV s^{-1}. As discussed before, the reformation of Na_xMoS_2 is a multiphase reaction between

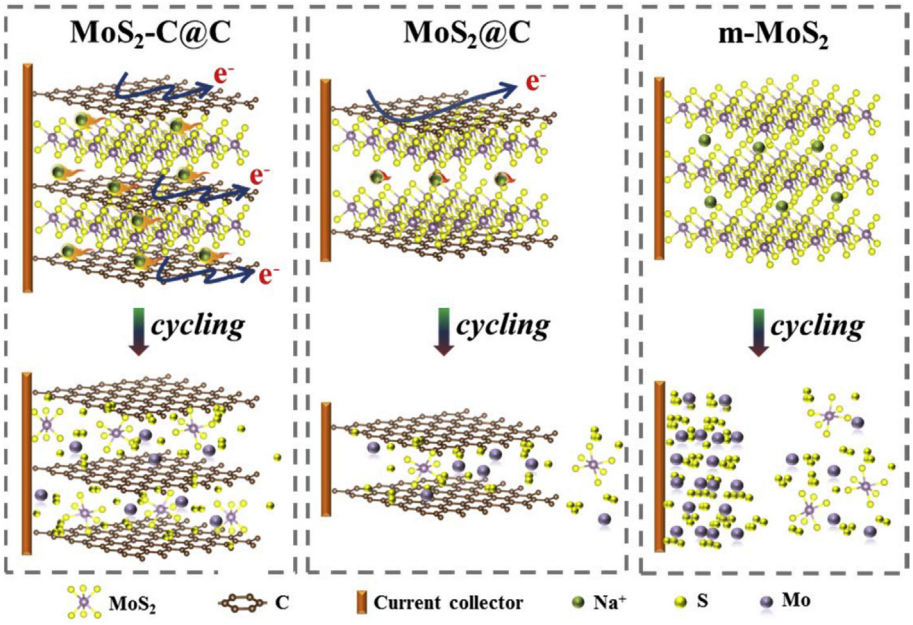

Fig. 7. Schematic illustration of the structural advantages of MoS_2-C@C for Na storage.

metallic Mo and amorphous Na_2S, and thus usually with low reaction efficiency. According to the literature [36], this process requires a small particle size and a good electric conductivity of the MoS_2 composite, which is just the case of the MoS_2-C@C sample. In Fig. 6a, the ratio of the two oxidation peaks maintains roughly the same with increasing scan rate. All the results demonstrate the absence of any significant kinetic limitations in the MoS_2-C@C electrode. For comparison, the MoS_2@C and *m*-MoS_2 electrodes obviously suffer from sluggish kinetics, resulting in the lack of the reformation peaks and the deformation of the CV curves (Fig. S12). Based on a power law relation ($I = a\,v^b$, where I is the current and *v* represents the scan rate), the charge storage mechanism can be identified based on the b value [49]. As shown in Fig. 6b, the b values of the redox peaks are larger than 0.9, suggesting favourable capacitive kinetics for MoS_2-C@C. The capacitive contribution at different scan rates is quantitatively analysed to be 62%–95% for increasing scan rates from 0.1 to 10 mV s^{-1}, as shown in Fig. 6c. The ultra-high pseudocapacitive contribution is indicative of fast kinetics, leading to superior rate performance.

The fast kinetics is also evidenced by the electrochemical impedance spectroscopy (EIS) measurements. In Fig. 6d, the EIS curves of the three samples exhibit similar profiles before cycling, with a semicircle in the high-to-medium frequency range and a slope in the low frequency range. The main difference is the diameter of the semicircle, corresponding to the charge transfer resistance (R_2), which is much smaller for MoS_2-C@C (165 Ω) than for the other two samples (382 Ω, and 1706 Ω for MoS_2@C, and *m*-MoS_2, respectively). This difference is also observed after charge-discharge cycling (cf. Fig. S13). The R_{ct} of the MoS_2-C@C electrode decreases upon cycling, staying at less than 20 Ω after the 50^{th} cycle, while it increases from the 1st cycle to the 50^{th} cycle to ~60 Ω for MoS_2@C, and is above 250 Ω in all cycles for *m*-MoS_2. With a smaller R_{ct}, the electron transfer in the MoS_2-C@C electrode is largely boosted during electrochemical processes.

Taking the structure into account, the MoS_2-C@C inter-overlapped structure is indeed favourable for reversible and fast Na storage, which is illustrated schematically in Fig. 7. On the one hand, the interfacial engineering results in the largest possible MoS_2:C interface, which provides effective local protection for MoS_2 and its redox products. Specifically, the flexible carbon matrix may serve as a barrier, preventing the pulverized active materials from peeling off from the electrode during the continuous volume change upon cycling. The strong physical confinement of carbon matrix could also maintain the contact between the reduction products (metallic Mo and amorphous Na_2S) as they form, and retard their aggregation, thus prompting the reformation of the Na_xMoS_2 and MoS_2 during charging process. In addition, the *in situ* protection of the multilayer heterointerfaces may hinder the soluble sodium polysulfides from dissolving into the electrolyte and further shuttling to the anode, via both physical confinement and chemical adsorption. The physical confinement of the carbon layers in MoS_2-C@C could be implied from the *in situ* Raman spectra in Fig. 4. When charging the cell to 2.55 V, both E^1_{2g} and A_{1g} peaks of 2H-MoS_2 reappear with the peak difference recover to ~21 cm^{-1}, which corresponds to 1–2 layers of MoS_2. This result may suggest that the redox reactions take place in-between the carbon layers. Otherwise, multiple layered MoS_2 is supposed to form in a more free space. With the multiple functionalities of the heterointerfaces, the capacity fading due to the loss of the active material is strongly alleviated, resulting in a durable Na storage. On the other hand, the carbon layers expand the interlayer spacing of MoS_2, allowing for fast Na^+ diffusion and offering abundant electron transfer routes, which promote the electron transfer rate. In combination, this leads to an ultrafast kinetics. In contrast, the MoS_2@C sample only features a surficial carbon coating with a single layer heterointerface, which provides only limited protection. Nevertheless, it exhibits an improved electrochemical performance compared to the *m*-MoS_2 sample, which has no carbon protection at all. For the latter, the fast capacity fading is predictable as the active material degrades and quickly transfers into the electrolyte. The *ex situ* SEM images of the electrodes after 400 cycles at 0.5 A g^{-1} in Fig. S14 give direct evidence of the carbon protection effect. In the MoS_2-C@C electrode, the layered structure is still preserved in general, but there are already lots of small nanoparticles appearing on the MoS_2@C electrode. For the *m*-MoS_2 electrodes, we could only find the nanoparticles which can easily detach from the electrode, causing capacity losses. Further post mortem study of the MoS_2-C@C electrode also supports the conclusion. Due to large volume change during repeated cycling, amorphization of the MoS_2 species cannot be avoided, which is also the case in our material. XRD patterns of both charged and discharged electrodes in Fig. S15a suggest completely amorphous structure of active material. In Figs. S15b–d, the HR-TEM image and HAADF-STEM image of the charged electrode present irregular morphology, while the corresponding SAED pattern shows a disordered structure of the Mo species. In the SAED patterns, the only weak diffraction rings can be

indexed as disordered graphitic carbon. The EDX (Fig. S15e) together with the STEM image indicate a homogeneous Mo distribution in the carbon matrix, that the loss of active material can be effectively inhibited. All the results highlight the significant role of the carbon component in the inter-overlapped structure for a durable electrochemical cycling by trapping the redox species and maintaining the structural integrity of the electrode.

Besides, from the crystallinity point of view, the regulating effect of dopamine in the MoS_2 formation leads to small size and few layer feature of the product. Consequently, the charge and ion transfer distance in the MoS_2-C@C is reduced, further improving the kinetics.

4. Conclusions

In summary, a MoS_2-C@C inter-overlapped structure has been designed and prepared through an interfacial engineering approach. The concurrent complexation of Mo(VI) to dopamine and self-polymerization of dopamine enables an architecture with alternative stacking of MoS_2 and carbon, which provides multilayer MoS_2:C heterointerfaces. As a result, the superstructure exhibits an ultra-long cycling stability (312 mA h g^{-1} at 2 A g^{-1} for 1000 cycles) and excellent rate capability (164 mA h g^{-1} at 20 A g^{-1} and 51 mA h g^{-1} at 50 A g^{-1}). With its outstanding performance, the MoS_2-C@C electrode is not only superior to the electrode with MoS_2@C (surface carbon coating) and *m*-MoS_2 (no carbon) studied in this work, but also shows better results than most state-of-the-art MoS_2/C-based SIB electrodes. The mechanistic investigations indicate that the fast kinetics and long cycling lifetime of the MoS_2-C@C electrode are related to the multi-functional heterointerfaces. The large MoS_2:C interface offers *in situ* protection for both the MoS_2 fragments and the polysulfide species, which alleviates the loss of active material and the capacity decay. The carbon matrix also impedes the agglomeration of the nanosized redox products via physical confinement, enhancing the reversibility of the electrochemical reactions. Furthermore, the carbon layers in between the MoS_2 layers provide additional electron transfer pathways, leading to faster redox reactions. Notably, the interfacial engineering strategy and the synthesis route have great potential to be extended to construct other transition metal based superstructures.

Data availability

The raw/processed data required to reproduce these findings cannot be shared at this time as the data also forms part of an ongoing study.

Author contributions

The manuscript was written with contributions of all authors. All authors have given approval to the final version of the manuscript.

Acknowledgements

This study is supported by the Bundesministerium für Bildung und Forschung (BMBF) of Germany via the “MagS” project (03XP0032A). This work contributes to the research performed at CELEST (Center for Electrochemical Energy Storage Ulm-Karlsruhe) and is funded by the German Research Foundation (DFG) under Project ID 390874152 (POLiS Cluster of Excellence). K. W. acknowledges financial support by the Chinese Scholarship Council (No.201706240159).

Appendix A. Supplementary data

Supplementary data to this article can be found online at https://doi.org/10.1016/j.ensm.2019.05.042.

References

[1] M. Armand, J.M. Tarascon, Nature 451 (2008) 652–657.
[2] P. Simon, Y. Gogotsi, B. Dunn, Science 343 (2014) 1210.
[3] N.-S. Choi, Z. Chen, S.A. Freunberger, X. Ji, Y.-K. Sun, K. Amine, G. Yushin, L.F. Nazar, J. Cho, P.G. Bruce, Angew. Chem. Int. Ed. 51 (2012) 9994–10024.
[4] H.D. Yoo, E. Markevich, G. Salitra, D. Sharon, D. Aurbach, Mater. Today 17 (2014) 110–121.
[5] A. Manthiram, J. Phys. Chem. Lett. 2 (2011) 176–184.
[6] C. Vaalma, D. Buchholz, M. Weil, S. Passerini, Nat. Rev. Mater. 3 (2018) 18013.
[7] R. Shannon, Acta Crystallogr. A 32 (1976) 751–767.
[8] X. Xu, M. Yan, X. Tian, C. Yang, M. Shi, Q. Wei, L. Xu, L. Mai, Nano Lett. 15 (2015) 3879–3884.
[9] C. Zhao, C. Yu, B. Qiu, S. Zhou, M. Zhang, H. Huang, B. Wang, J. Zhao, X. Sun, J. Qiu, Adv. Mater. 30 (2018) 1702486.
[10] Y. Xiao, S.H. Lee, Y.-K. Sun, Adv. Energy Mater. 7 (2016) 1601329.
[11] S.-H. Yu, X. Feng, N. Zhang, J. Seok, H.D. Abruña, Accounts Chem. Res. 51 (2018) 273–281.
[12] C. Zhu, X. Mu, P.A. vanAken, Y. Yu, J. Maier, Angew. Chem. Int. Ed. 53 (2014) 2152–2156.
[13] J. Yang, X. Zhou, D. Wu, X. Zhao, Z. Zhou, Adv. Mater. 29 (2016) 1604108.
[14] K. Zhang, M. Park, L. Zhou, G.-H. Lee, W. Li, Y.-M. Kang, J. Chen, Adv. Funct. Mater. 26 (2016) 6728–6735.
[15] J. Wang, C. Luo, T. Gao, A. Langrock, A.C. Mignerey, C. Wang, Small 11 (2014) 473–481.
[16] J. Xu, J. Zhang, W. Zhang, C.-S. Lee, Adv. Energy Mater. 7 (2017) 1700571.
[17] L. David, R. Bhandavat, G. Singh, ACS Nano 8 (2014) 1759–1770.
[18] P. Xiong, R. Ma, N. Sakai, L. Nurdiwijayanto, T. Sasaki, ACS Energy Lett. 3 (2018) 997–1005.
[19] H. Jiang, D. Ren, H. Wang, Y. Hu, S. Guo, H. Yuan, P. Hu, L. Zhang, C. Li, Adv. Mater. 27 (2015), 3582-3582.
[20] C. Zhao, C. Yu, M. Zhang, Q. Sun, S. Li, M. Norouzi Banis, X. Han, Q. Dong, J. Yang, G. Wang, X. Sun, J. Qiu, Nano Energy 41 (2017) 66–74.
[21] A.K. Geim, I.V. Grigorieva, Nature 499 (2013) 419–425.
[22] R. Wang, S. Wang, X. Peng, Y. Zhang, D. Jin, P.K. Chu, L. Zhang, ACS Appl. Mater. Interfaces 9 (2017) 32745–32755.
[23] Z. Lei, J. Zhan, L. Tang, Y. Zhang, Y. Wang, Adv. Energy Mater. 8 (2018) 1703482.
[24] C. Zhao, X. Wang, J. Kong, J.M. Ang, P.S. Lee, Z. Liu, X. Lu, ACS Appl. Mater. Interfaces 8 (2016) 2372–2379.
[25] Z. Li, A. Ottmann, Q. Sun, A.K. Kast, K. Wang, T. Zhang, H.-P. Meyer, C. Backes, C. Kübel, R.R. Schröder, J. Xiang, Y. Vaynzof, R. Klingeler, J. Mater. Chem. A 7 (2019) 7553–7564.
[26] F. Ma, A. Yuan, J. Xu, P. Hu, ACS Appl. Mater. Interfaces 7 (2015) 15531–15541.
[27] E. Karabulut, T. Pettersson, M. Ankerfors, L. Wågberg, ACS Nano 6 (2012) 4731–4739.
[28] M.J. Harrington, A. Masic, N. Holten-Andersen, J.H. Waite, P. Fratzl, Science 328 (2010) 216.
[29] H. Zeng, D.S. Hwang, J.N. Israelachvili, J.H. Waite, Proc. Natl. Acad. Sci. Unit. States Am. 107 (2010) 12850.
[30] C. Zhao, J. Kong, L. Yang, X. Yao, S.L. Phua, X. Lu, Chem. Commun. 50 (2014) 9672–9675.
[31] P. Joensen, E.D. Crozier, N. Alberding, R.F. Frindt, J. Phys. C Solid State Phys. 20 (1987) 4043.
[32] A. Midya, A. Ghorai, S. Mukherjee, R. Maiti, S.K. Ray, J. Mater. Chem. A 4 (2016) 4534–4543.
[33] J. Xie, J. Zhang, S. Li, F. Grote, X. Zhang, H. Zhang, R. Wang, Y. Lei, B. Pan, Y. Xie, J. Am. Chem. Soc. 135 (2013) 17881–17888.
[34] C. Lee, H. Yan, L.E. Brus, T.F. Heinz, J. Hone, S. Ryu, ACS Nano 4 (2010) 2695–2700.
[35] K. Kobayashi, J. Yamauchi, Phys. Rev. B 51 (1995) 17085–17095.
[36] S. Hao, X. Shen, M. Tian, R. Yu, Z. Wang, L. Chen, Nano Energy 41 (2017) 217–224.
[37] X. Zhang, X.-F. Qiao, W. Shi, J.-B. Wu, D.-S. Jiang, P.-H. Tan, Chem. Soc. Rev. 44 (2015) 2757–2785.
[38] X. Xie, T. Makaryan, M. Zhao, K.L. Van Aken, Y. Gogotsi, G. Wang, Adv. Energy Mater. 6 (2016), 1502161-n/a.
[39] J. Park, J.-S. Kim, J.-W. Park, T.-H. Nam, K.-W. Kim, J.-H. Ahn, G. Wang, H.-J. Ahn, Electrochim. Acta 92 (2013) 427–432.
[40] S.H. Choi, Y.N. Ko, J.-K. Lee, Y.C. Kang, Adv. Funct. Mater. 25 (2015) 1780–1788.
[41] Y. Pang, S. Zhang, L. Liu, J. Liang, Z. Sun, Y. Wang, C. Xiao, D. Ding, S. Ding, J. Mater. Chem. A 5 (2017) 17963–17972.
[42] X. Xu, D. Zhou, X. Qin, K. Lin, F. Kang, B. Li, D. Shanmukaraj, T. Rojo, M. Armand, G. Wang, Nat. Commun. 9 (2018) 3870.
[43] X. Xu, R. Zhao, W. Ai, B. Chen, H. Du, L. Wu, H. Zhang, W. Huang, T. Yu, Adv. Mater. 30 (2018) 1800658.
[44] P. Zhang, F. Qin, L. Zou, M. Wang, K. Zhang, Y. Lai, J. Li, Nanoscale 9 (2017) 12189–12195.
[45] W. Ren, H. Zhang, C. Guan, C. Cheng, Adv. Funct. Mater. 27 (2017) 1702116.
[46] S. Kalluri, K.H. Seng, Z. Guo, A. Du, K. Konstantinov, H.K. Liu, S.X. Dou, Sci. Rep. 5 (2015) 11989.
[47] T.S. Sahu, Q. Li, J. Wu, V.P. Dravid, S. Mitra, J. Mater. Chem. A 5 (2017) 355–363.
[48] L. Fan, R. Ma, Y. Yang, S. Chen, B. Lu, Nano Energy 28 (2016) 304–310.
[49] V. Augustyn, J. Come, M.A. Lowe, J.W. Kim, P.-L. Taberna, S.H. Tolbert, H.D. Abruña, P. Simon, B. Dunn, Nat. Mater. 12 (2013) 518.